# Theoretical study of laser-induced ultrafast spin dynamics in small iron-benzene clusters and of related laser and magnetic-field effects

Hong Du,[1] Jing Liu,[2] Na Zhang,[1] Jun Chang,[1] Wei Jin,[1,*] Chun Li,[3] Georgios Lefkidis,[2,3,†] and Wolfgang Hübner[2]

[1]*School of Physics and Information Technology, Shaanxi Normal University, Xi'an 710119, China*

[2]*Department of Physics and Research Center OPTIMAS, Technische Universität Kaiserslautern, PO Box 3049, 67653 Kaiserslautern, Germany*

[3]*School of Mechanics, Civil Engineering and Architecture, Northwestern Polytechnical University, Xi'an 710072, China*

(Received 24 December 2018; revised manuscript received 11 March 2019; published 22 April 2019)

Using high-level quantum chemistry calculations, we predict various ultrafast laser-induced spin dynamics scenarios in clusters $Fe_mBz_n$ ($m, n = 1, 2$) based on the nonadiabatic $\Lambda$ process—an indirect transition channel from the initial state to the final state through the participation of several spin-mixed intermediate states. The geometry-dependent electronic structures of the four clusters are found to exhibit distinct characteristics, and prove to strongly affect the laser parameters and dynamical behavior of the spin-flip scenarios. For the two Fe-dimer clusters, a charge-transfer state involving spin-transfer scenario is achieved in $Fe_2Bz$, which turns to be much faster than the ordinary one obtained in $Fe_2Bz_2$, and thus is considered to be promising for future spintronics applications. Furthermore, to provide valuable information for the measurement and implementation of the ultrafast magnetism response, the effects of the full width at half maximum (FWHM) of the laser pulse and the magnitude of the external magnetic field on the proposed spin scenarios are investigated. The analysis of the stability and sensitivity of each scenario shows that the spin-transfer scenarios have smaller tolerance values than spin-flip scenarios with respect to the laser FWHM, and a desired spin scenario is only possible when the magnetic field strength lies in a moderate region. The latter effect enables us to obtain the lateral resolution of the device sample for its possible memory usage and to reach the complementary metal oxide semiconductor scale, beyond the optical resolution limit. All the results in this paper contribute a further step toward the experimental realization of our spin dynamics and their future nanospintronics applications.

DOI: 10.1103/PhysRevB.99.134430

## I. INTRODUCTION

With the miniaturization of spintronics devices for high-density magnetic storage, the sizes of many systems have been reduced to molecular/atomic scale [1]. In this limit, benefitting from the quantum effects of the static and dynamic magnetic properties and the preservation of spin-coherence time [2], several molecular nanomagnets and spin-based quantum gates as well as their feasibility in quantum computing have been proposed [3–7]. Meanwhile, to meet the increasing demand for high-speed magnetic recording and information precessing, a variety of investigations on the laser-induced ultrafast spin dynamics, motivated by the observation of the demagnetization of ferromagnetic Ni within 2 ps in 1996 [8], have been reported [9–20]. Combining these two aspects, in attempts to realize ultrafast spin-based nanologic elements for constructing future molecular computers, the search for suitable molecular materials with the desired functionalities becomes a timely and appealing issue.

Since the discovery of ferrocene in the 1950s [21], iron-benzene (Fe-Bz) complexes have been investigated intensively due to their unique physical and chemical features in catalytic and biological processes, among which the (half-) sandwichlike species are of particular interest. Numerous experimental works [22–29] concerning their synthesis by use of the laser vaporization techniques and characterization by adopting the mass spectrometry and photo-dissociation/-ionization/-electron spectroscopy have been performed. On the theory side, considerable (common) density-functional-theory-based investigations [25,27,29–34] on the geometric, energetic, electronic, vibrational, and magnetic properties of these organometallic complexes have been reported successively. Especially, by elucidating the fundamental interactions between the $\pi$ − cloud and the $3d$ electrons that are responsible for different magnetism features, these gas phase (half-)sandwichlike Fe-Bz clusters can serve as prototypical systems for investigating more realistic complicated Fe-Bz complexes [35] and extended Fe-Bz-based structures (such as the systems adsorbing iron on/in coronene [29,36,37], pyrene [29,38], graphene [39,40], $C_{60}$ [24,36,41], and nanotube [42]), which are all technologically possible at present stage, thus bringing them closer to experimental realization. With respect to device applications, it has been demonstrated that robust and easy-to-prepare carbon-based substrates are well suited to adsorb transition metal (TM) dimers for the purpose of high-density magnetic recording [31]. Some one-dimensional TM-Bz sandwich polymers [43–45] (like V-Bz and Mn-Bz wires) are suggested to be ideal materials for promising spin-polarized transport since they exhibit half metallicity (one spin channel is metallic while the opposite spin channel is insulating) and the spin filter effect.

*jinwei@snnu.edu.cn
†lefkidis@physik.uni-kl.de

 

In this paper, we present the *ab initio* investigation of the laser-induced ultrafast spin dynamics in clusters $Fe_mBz_n$ $(m, n = 1, 2)$, the existence of which has been verified by experiment [26,28]), and the corresponding parameter effects on them. By exploring controllable ultrafast spin manipulation via the Λ process [46] in these four systems, we achieve various spin-flip scenarios and two special spin-transfer scenarios [a charge-transfer (CT) state involving one and a reversible one]. Here, as an indirect optical transition channel which consists of the excitation of the system from the initial state to the intermediate states by absorbing an incident photon and the successive de-excitation from the intermediate states to the final state by emitting a photon, the two-photon Λ process is typically orders of magnitude faster than the direct transition. This is especially the case for initial and final states with opposite spin directions, in which situation the direct transition is spin forbidden. The types of spin functionality are identified by the different magnetic properties of the initial and final states, e.g., spin flip for these two states possessing opposite spin directions and spin transfer for them having different spin localizations. These predictions are of significant interest and necessity because they can stimulate relevant experimental efforts and offer guidance for designing related spin functionality for future integrated spin-logic devices and quantum computers.

As extending systems of $Co_mBz_n^{(+/0)}$ $(m, n = 1, 2)$ [47], here we are not limited to just repeat the same kind of calculation for different structures and explore their unique electronic and magnetic properties, but also expect to establish systematic insights on the ultrafast spin dynamics of the TM-Bz systems through the investigation and step further to study the laser and magnetic field effects on spin dynamics for their future realization and promising applications. It has been reported in our earlier paper that iron centers are easier and more effective than Co to realize spin flip [48], while for spin transfer, homonuclear iron-oxide clusters are found to be more suitable than the corresponding cobalt ones since they are usually of lower symmetries [49] and thus are more likely to possess states with distinguishable spin localizations. As we will see later in this paper, except for $Fe_2Bz$, the other three clusters have lower symmetries than their corresponding cobalt clusters. Concerning the functionality, all four spin-flip scenarios achieved in $Fe_mBz_n$ $(m, n = 1, 2)$ (for which the effects of the TM atom and the Bz molecule on the level distributions and on the laser energies are similar to those in Co-Bzs) are reversible due to their clear-cut dynamical behavior, while only the flip dynamics in $Co_2Bz_{1,2}$ is reversible. Spin crossover has not been found in Fe-Bzs. However, a spin-transfer scenario involving CT states, as well as a reversible spin transfer are achieved in $Fe_2Bz$ and $Fe_2Bz_2$, respectively, neither of which is realized in $Co_2Bz$. These somewhat consistent but mainly distinct results suggest that the Fe-Bz systems are good candidates for the further revelation of the underlying ultrafast spin control in TM-Bz systems and for the subsequent investigation of the laser effect to compare spin-flip and -transfer scenarios and to guide their experimental implementation. With only one transfer process achieved, the Co-Bz systems are insufficient to give convincing remarks for the latter objective.

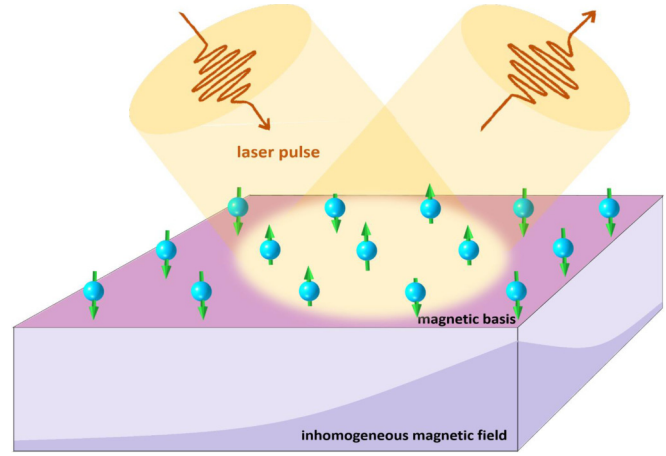


FIG. 1. Illustration of the magnetic field addressing. Within the same laser spot, the molecular ultrafast spin responses, obtained based on our two-photon Λ process, are dependent on the magnetic field strength. Thus, by applying an inhomogeneous magnetic field, the lateral resolution of the device sample can be obtained and utilized for the possible memory application.

Besides, the study of the magnetic field effect (B effect) is of strong promise due to its relevance in data storage and processing utilization. More specifically, as the spintronic devices are downsized to nanoscale, the spatial resolution becomes the main factor that hinders its practical applications. Since the magnetic field strength is one of the parameters that affects the fidelity of the laser-driven ultrafast spin dynamics achieved in this paper, we can exploit the B effect on certain spin dynamics and convert it to a lateral resolution of our spin process, through the introduction of an inhomogeneous magnetic field. As illustrated in Fig. 1, when applying a nonuniform magnetic field (instead of a uniform one which induces the same magnetization change everywhere) on a sample surface made of homogeneous Fe-Bz molecules, different locations (within the same laser spot) may have distinct spin responses (e.g., whether a spin-flip/-transfer process with desired fidelity is realized). Thus, from the magnetic-field values, one can distinguish the active region where an ultrafast magnetization change occurs from its surroundings, and obtain spatial resolution of a device volume for precise high-density storage and possible memory applications, which go beyond the optical resolution limit.

The organization of the paper is as follows. Section II introduces the computational method. The structures and electronic structures of the four systems are given in Sec. III. In Sec. IV, our main results are presented and discussed: First, some selective results of the achieved ultrafast dynamics (Sec. IV A), followed by the effects of laser FWHM (Sec. IV B) and B field (Sec. IV C). A summary is given in Sec. V.

## II. THEORY AND METHODS

For the first-principles study of our ultrafast spin dynamics, we start from the restricted Hartree-Fock (HF) calculation (to avoid spin contamination) for geometric optimization and infrared spectra by using the GAUSSIAN 16 package [50].

At this level, normally the threshold values of $4.5 \times 10^{-4}$ and $3.0 \times 10^{-4}$ Hartree/Bohr for the maximum component of the force and the root-mean-square (RMS) of the forces are chosen, respectively. Whenever small imaginary frequencies appear, even stricter criteria (i.e., with the values of $2 \times 10^{-6}$ and $1.0 \times 10^{-6}$ Hartree/Bohr, respectively) are applied. The convergence criterion of the self-consistent field procedure is set to $10^{-8}$, which in turn, means that the RMS change and the maximum density matrix change are less than $10^{-8}$ and $10^{-6}$, respectively, and the change value of energy is less than $10^{-6}$ Hartree. Note that for the values of bond lengths in Ångström and energies (or energy differences) in eV to be shown in the later part of this paper, the formats of the truncated five and four digits (which are just enough to distinguish the respective differences between different bonds and between different states) are chosen, respectively.

Based on the single-determinantal solution of the Schrödinger equation, we subsequently apply the symmetry-adapted cluster configuration interaction (SACCI) method [51] for the purpose of a more accurate description of the electronic structure of the system. At this step, by taking various multiple virtual excitations between molecular orbitals into account, the many-body ground and various excited electronic states (which are different superpositions of the many-body wave-function configurations with different coefficient sets determined by the variational method) are obtained. In this way, both static and dynamic correlations are nicely included. Both of them are crucial and well suited to describe laser-induced femtosecond dynamics since the former ones play a significant role in magnetization and the latter ones determine the optical activity of the system [52–54].

For the dynamical part, to distinguish between"spin-up" and "spin-down" states and to produce spin-mixed intermediate states that enable the indirect transition between the initial and final states as required by the Λ process, a static external magnetic field (with a strength of $10^{-5}$ atomic units, which proves to be a suitable value for producing appropriate Zeeman splittings, and for efficiently achieving the desired dynamics in our previous work) and the spin-orbit coupling (for which the two-electron contributions are accounted for by the effective nuclear charges) are perturbatively added. Then, under the influence of the well-tailored laser pulse, the time evolution of the system, described by a set of coupled differential equations, is solved with the fifth-order Runge-Kutta method with Cash-Karp adaptive step size [55]. During this procedure, a specially developed genetic algorithm [56] is applied to optimize the laser pulses and efficiently get the desired spin scenario. More details can be found in Refs. [48,49,57].

## III. STRUCTURES AND ENERGY LEVELS

The four optimized structures at the HF level are shown in Fig. 2, in which their symmetries and spin multiplicities are indicated. Considering the balance between calculation cost and accuracy for such strongly correlated systems, we choose the Lanl2dz basis set for the Fe atom and STO-3G for the C and H atoms as a compromise. In each optimization, several candidate structures were fully optimized (without imposing symmetry constraints) under different spin

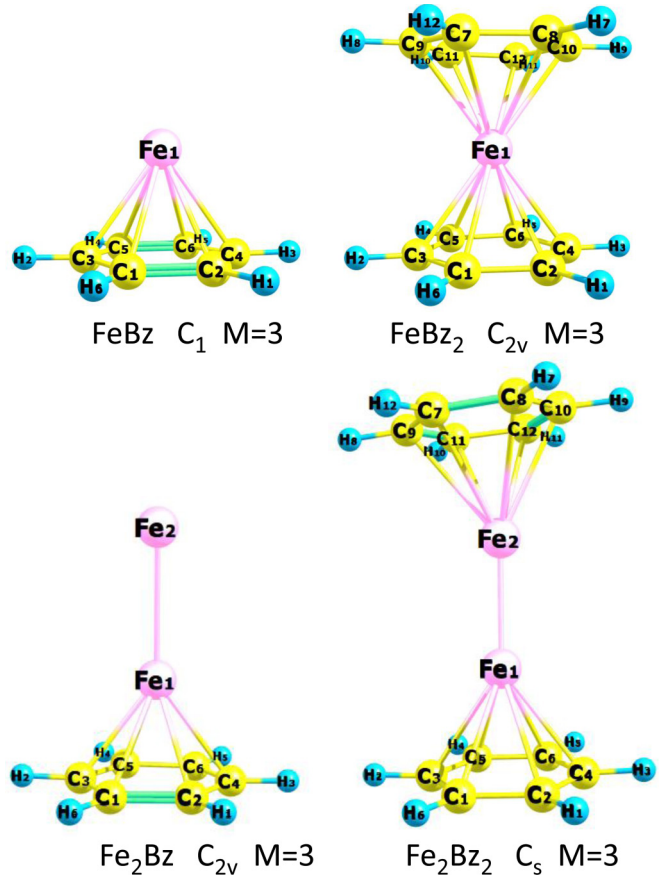


FIG. 2. The optimized geometries of FeBz, $FeBz_2$, $Fe_2Bz$, $Fe_2Bz_2$ as well as their symmetries and spin multiplicities.

multiplicities, and subsequent harmonic frequency approximation calculations were performed to confirm that the optimized geometry corresponds to a minimum. It turns out that the ground-state geometries of all four structures take the form of triplet half-sandwich or sandwich type, with the symmetries of $C_1$, $C_{2v}$, $C_{2v}$, and $C_s$, respectively. Clearly, except for $Fe_2Bz$, the other three clusters have lower symmetries than the corresponding Co-Bzs [47] resulting from the unique nature of Fe. This finding is consistent with the statement that iron oxides are lower in symmetry than the corresponding cobalt-oxides in Ref. [49]. Details concerning the comparisons of ground-state structures with other work and the analysis of the structural parameters and some vibrational modes are given in the Appendix.

The lowest 91 ground and excited energy levels of the four structures after the inclusion of SOC and external magnetic field are shown in Fig. 3, in which the initial and final states that involve the spin dynamics to be discussed later are marked. Comparing the four electronic structures in Fig. 3, we find that with an additional Fe atom the *d* states (e.g., below 1.5 eV) of the Fe dimer clusters (i.e., $Fe_2Bz$ and $Fe_2Bz_2$) are more than that of the respective FeBz and $FeBz_2$ clusters, and with an additional Bz molecule the high-lying CT states (e.g., above 2 eV) of $FeBz_2$ and $Fe_2Bz_2$ are more than that of the respective mono Bz clusters (i.e., FeBz and $Fe_2Bz$). This is consistent with the findings in Ref. [47]. We attribute them to the stronger 3*d* electron correlations introduced by the

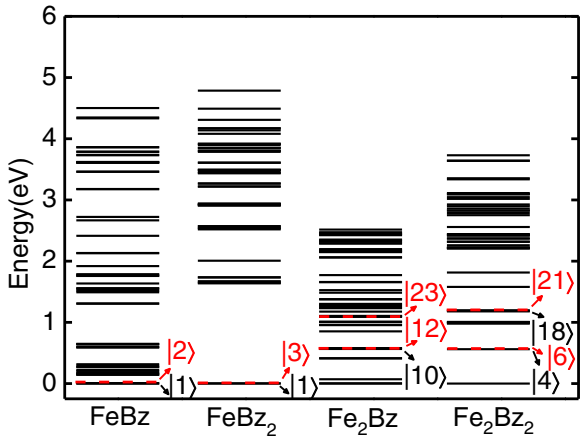


FIG. 3. Low-lying energy levels of the four structures obtained from the SACCI method. The initial and final states that involve the spin dynamics to be discussed later are marked.

additional Fe atom and the inductive-*I* effect of Bz that gives rise to stronger $3d$-$\pi$ electron interactions, respectively. The latter effect can be obviously noticed from the ground-state Mulliken atomic charge-density values of the clusters FeBz ($-0.52$ in Bz, 0.52 in Fe, as listed in Table I) and $FeBz_2$ ($-0.32$ in Bz1, $-0.32$ in Bz2, and 0.64 in Fe, as listed in Table I) and those of the clusters $Fe_2Bz$ ($-0.59$ in Bz, 0.20 in Fe1, and 0.40 in Fe2) and $Fe_2Bz_2$ ($-0.58$ in Bz1, $-0.57$ in Bz2, 0.32 in Fe1, and 0.83 in Fe2). In both cases, the charge-density values for Fe atoms increase, resulting from the attraction of electrons by the additional Bz. Similar to the cases of $Co_mBz_n^{(+/0)}$ ($m, n = 1, 2$) [47], the distinct level distributions of the four structures would induce different dynamics behavior and laser parameters. At least for the same type of spin-dynamics (e.g., spin-flip scenario), it can be speculated that most probably the laser energies for driving the spin dynamics in Fe-Bzs will be higher than that for the corresponding $Fe_2$-Bzs, and the laser energies for driving the spin dynamics in $Fe_{1,2}Bz$ half sandwiches will be lower than that for corresponding sandwichlike structures $Fe_{1,2}Bz_2$.

## IV. LASER-INDUCED ULTRAFAST SPIN DYNAMICS

### A. Spin-flip and -transfer scenarios

By choosing appropriate initial and final states under different sets of laser parameters, spin-flip scenarios, with final occupation of the target state (i.e., fidelity) 98.8%, 97.0%, 98.6%, and 98.7%, respectively, are all achieved in the four structures. The information of the initial and final states (of which the energetic positions are marked in Fig. 3), including their energies, spin expectation values, spin density, and charge density is listed in Table I. Depending on the directions of the external magnetic fields, as shown in Table I, the $x-$, $z-$, $z-$, and $y-$component of the spin gets flipped, respectively. Consistent with other flip dynamics achieved in our previous work, all four flip scenarios exhibit symmetric behavior resulting from the fact that the two branches of the $\Lambda$ process always have comparable transition magnitudes due to the similar electronic properties of the initial and final states. Here, considering the fact that there are no novel features in the dynamics behavior for the obtained spin-flip scenarios and extensively related conclusive remarks have been addressed in our previous papers [40,47,49], they are not shown in this paper. It should be noted that, due to the higher symmetries of the clusters $FeBz_2$ and $Fe_2Bz$, there are actually 121 states calculated for spin dynamics. The lowest 91 of them in Fig. 3 are only shown for comparison reason.

The corresponding optimized laser parameters are listed in Table II. As surmised from the discussion of the level distributions in the last subsection, with more Bzs, the laser energies for driving spin-flip scenarios in $FeBz_2$ (2.465 eV) and $Fe_2Bz_2$ (1.158 eV) are, respectively, higher than that for FeBz (0.195 eV) and $Fe_2Bz$ (0.626 eV). Naturally, it is the cluster $FeBz_2$ with fewer Fe atoms and more Bz molecules that requires the highest laser energy for driving its spin-flip

TABLE I. Direction of the external magnetic field and information of the initial and final states (including their energies, spin expectation values, spin density, and charge density) for the spin scenarios discussed in this paper. Here Bz1 and Bz2 refer to the bottom and upper benzene rings, respectively.

| Structure | Scenario | Initial and final states | Energy (eV) | $\langle S_x\rangle$ | $\langle S_y\rangle$ | $\langle S_z\rangle$ | Spin density Fe1 | Spin density Fe2 | Charge density Fe1 | Charge density Fe2 | Charge density Bz1 | Charge density Bz2 |
|---|---|---|---|---|---|---|---|---|---|---|---|---|
| FeBz | flip | state 1 | 0.000 | −0.90 | 0.00 | 0.00 | −1.96 | – | 0.52 | – | −0.52 | – |
| | (B: $\theta = 90°, \phi = 0°$) | state 2 | 0.001 | 0.90 | 0.00 | 0.00 | 1.96 | – | 0.52 | – | −0.52 | – |
| $FeBz_2$ | flip | state 1 | 0.000 | 0.00 | 0.00 | −0.71 | −1.96 | – | 0.64 | – | −0.32 | −0.32 |
| | (B: $\theta = 0°, \phi = 90°$) | state 3 | 0.001 | 0.00 | 0 | 0.71 | 1.96 | – | 0.64 | – | −0.32 | −0.32 |
| | (i) flip | state 10 | 0.563 | 0.00 | 0.00 | −0.83 | −0.27 | −1.73 | 0.08 | 0.49 | −0.57 | – |
| | (B: $\theta = 0°, \phi = 90°$) | state 12 | 0.564 | 0 | 0.00 | 0.83 | 0.27 | 1.73 | 0.08 | 0.49 | −0.57 | – |
| $Fe_2Bz$ | (ii) transfer | state 12 | 0.564 | 0.00 | 0.00 | 0.83 | 0.27 | 1.73 | 0.08 | 0.49 | −0.57 | – |
| | (B: $\theta = 0°, \phi = 90°$) | state 23 | 1.005 | 0 | 0 | 0.72 | 2.00 | −0.06 | 0.30 | 0.30 | −0.61 | – |
| | (i) flip | state 4 | 0.561 | −0.12 | −0.73 | 0.00 | −0.03 | −1.94 | 0.48 | 0.70 | −0.61 | −0.58 |
| | (B: $\theta = 90°, \phi = 90°$) | state 6 | 0.562 | −0.12 | 0.71 | 0.00 | 0.03 | 1.94 | 0.48 | 0.70 | −0.61 | −0.58 |
| $Fe_2Bz_2$ | (ii) transfer | state 18 | 1.177 | −0.03 | 0.20 | 0.65 | 0.08 | 1.86 | 0.55 | 0.61 | −0.61 | −0.55 |
| | (B: $\theta = 45°, \phi = 90°$) | state 21 | 1.197 | 0.06 | 0.73 | 0.03 | 1.81 | 0.09 | 0.56 | 0.63 | −0.59 | −0.60 |

TABLE II. The optimized parameters of the laser pulses for the achieved ultrafast spin scenarios. Here, $\theta$ and $\phi$ denote the angles of the incidence in spherical coordinates, and $\gamma$ is the angle between the polarization of the light and the optical plane. FWHM is the full width at half maximum of the laser pulse.

| Structure | Scenario | Fidelity | Laser parameters | | | | | |
|---|---|---|---|---|---|---|---|---|
| | | | $\theta(^\circ)$ | $\phi(^\circ)$ | $\gamma(^\circ)$ | Intensity (J s$^{-1}$ m$^{-2}$) | FWHM(fs) | Energy(eV) |
| FeBz | flip | 98.8% | 227.7 | 348.4 | 144.3 | 7.82 | 500 | 0.195 |
| $FeBz_2$ | flip | 97.0% | 45.0 | 15.1 | 310.7 | 2.37 | 500 | 2.465 |
| $Fe_2Bz$ | (i) flip | 98.6% | 17.2 | 167.2 | 213.9 | 0.14 | 94 | 0.626 |
| | (ii)transfer | 86.7% | 211.1 | 138.7 | 189.7 | 0.14 | 158 | 0.594 |
| $Fe_2Bz_2$ | (i) flip | 98.7% | 211.8 | 284.0 | 32.7 | 0.14 | 226 | 1.158 |
| | (ii) transfer | 84.1% | 90.1 | 58.8 | 189.0 | 2.35 | 594 | 2.185 |

scenario due to its fewer $d$ states and more CT states. Detailed analysis shows that there are 21 intermediate states involved, which is the largest number among all the spin scenarios in this paper. These are consistent with the findings for Co-Bz clusters [47]. One exception is that, instead of $Fe_2Bz$, which has more $d$ states, it is the cluster FeBz that requires the lowest laser energy for flipping spin. The reason is that the initial and final states for spin flip in FeBz are the ground states, nearby which are intensive candidate intermediate states. It shows that there are only three intermediate states (states 9, 10, and 11 with energies 0.179, 0.206, and 0.207 eV, respectively) involved in this scenario, leading to a small laser energy 0.195 eV (which is nearly resonant to the energy difference between the initial/final state and the highest-lying involved intermediate state). While for the flip scenario in $Fe_2Bz$, with states 10 and 12 being the initial and final states, respectively, only three intermediate states (i.e., states 1, 2, and 11, with energies 0, 0.0003, and 0.564 eV, respectively) are involved. The energy difference between initial/final and the lowest intermediate states is larger, thus causing a higher laser energy.

Interestingly, it is found that, for each flip scenario, by exchanging the initial and final states and using the same optimized laser parameters, an almost equivalent fidelity of the process can also be achieved. The first reason for this reversibility can be ascribed to the easiest and most efficient nature of Fe atoms with respect to the ultrafast magnetization control as stated in Ref. [48]. As shown in this study, the four flip scenarios achieved in Fe-Bzs all require lower laser energies but with higher fidelity values, compared to the corresponding ones in Co-Bzs [47]. The other one is due to the symmetric features of the flip scenarios since their quasidegenerate initial and final states originating from the same triplet term normally ensure the similar transition properties of the two branches (initial-intermediate branch and intermediate-final branch) of the $\Lambda$ process. Under the influence of the same laser parameters, the originally similar transition magnitudes and dynamics behavior with time involution as well as the high fidelity achieved of the scenario makes the system easily go backward. However, for Co-Bz systems [47], our present study shows that only two flip scenarios in $Co_2Bz$ and $Co_2Bz_2$ are reversible, due to the smaller number of intermediate states involved and the relatively simpler dynamical behavior.

In addition, spin-transfer scenarios with fidelity 86.7% and 84.1% on the two Fe dimer clusters are also achieved, as shown in Fig. 4. The information of the corresponding initial and final states and the optimized laser parameters can be seen in Tables I and II, respectively. For the first transfer scenario [Fig. 4(a)], detailed inspection shows that it does not only alter spin localization from Fe2 to Fe1, but also shifts electron density from Fe1 to Fe2, in the opposite direction of the spin transfer. Here, an noticeable increase of the charge density on Fe1 can be observed when comparing the charge-density values of states 12 and 23 in Table I, indicating there is a loss of electrons on this atom. This simultaneous charge and spin density transfer is quite promising for future spintronics applications. For the second laser-driven transfer scenario [Fig. 4(b)], with a B field along the direction of the angle

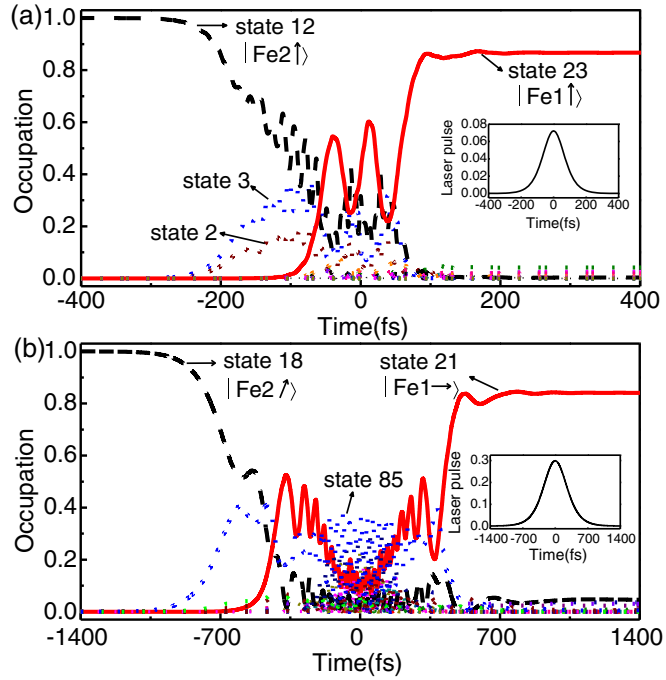


FIG. 4. Spin-transfer scenarios in clusters (a) $Fe_2Bz$ and (b) $Fe_2Bz_2$, respectively. For each scenario, the main panel depicts the time-resolved occupation of the involved states (initial: dashed, final: solid, intermediate: others), and the inset one shows the envelope of the optimized laser pulse.

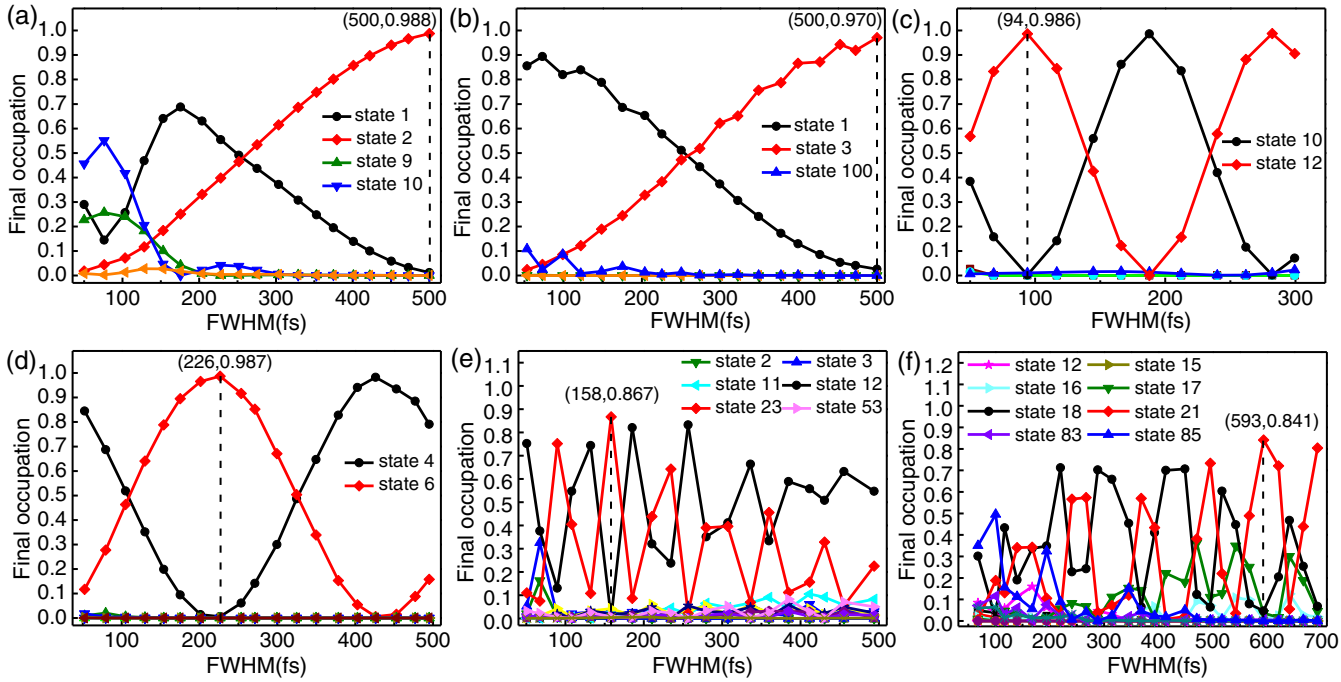


FIG. 5. The FWHM effect on the six spin scenarios discussed in this paper. (a)–(d) give the FWHM-dependent final occupation of the involved states of the spin-flip processes in FeBz, $FeBz_2$, $Fe_2Bz$, and $Fe_2Bz_2$, respectively, and (e) and (f) show the FWHM-dependent final occupation of the involved states of the spin-transfer processes in $Fe_2Bz$ and $Fe_2Bz_2$, respectively. In each subfigure, the lines connected by solid circles and diamonds represent the change trends of the initial and final states, respectively, and others denote the FWHM-dependent final occupation of some selected intermediate states which show noticeable occupation during the spin dynamics. The vertical dashed lines denote the optimized pulse durations ($FWHM_R$).

bisector of the $y-z$ plane (i.e., $\theta = 45°, \phi = 90°$), the $y-$ and $z-$ spin components of the system are exchanged. In addition, this transfer scenario is found to be reversible, i.e., under the influence of the same laser parameters, the initially occupied state 21 can be transferred to the finally occupied state 18 with occupation of 83.2%, analogous to the "toggle" switching in the ferrimagnetic alloy GdFeCo [11]. The reversibility can be traced back to the closely lying initial and final states which enable the intermediate states to be both optically accessible from them in a balanced manner (based on the fact that the total 23 intermediate states involved in the reversed scenario are exactly the same as the ones in the original scenario) and the almost symmetric behavior of the original dynamics with respect to the time inversion [as can be seen in Fig. 4(b)]. While for the scenario Fig. 4(a) in which the energetically distant initial and final states stem from different triplet terms, the relative low fidelity and asymmetric dynamics behavior indicate the unbalanced branches of the $\Lambda$ process and thus result in its irreversibility. Another difference between the two transfer scenarios lies in the dynamics timescales. The time duration required by the scenario shown in Fig. 4(a) to realize the CT states involving spin transfer is around 500 fs, which is much faster than that (around 2000 fs) required by Fig. 4(b). This is expected since the CT excitations are normally faster than the $dd$ transitions.

### B. Effect of laser FWHM on ultrafast spin dynamics

To offer further guidance for experimental implementation, it is important to examine the influence of the the laser parameters on the achieved spin scenarios. The effects of laser detuning (i.e., the deviation from the resonant laser energy) and angle resolution (i.e., the deviation from the optimized laser orientations) have been investigated in our previous papers [53,58,59]. It has been shown that the laser pulse duration has a substantial effect on the correlation between the magnetic and optical responses for femtosecond magnetism [60]. Thus, it is of necessity for us to go further to study the FWHM effect on the aforementioned six spin scenarios, aiming at assessing their experimental adaptability and thus providing closer connections to experiments.

The change trends of the dynamics fidelity when the laser FWHM deviates from their respective resonant FWHM ($FWHM_R$, marked with black dashed lines) while keeping other laser parameters (i.e., angles, intensity, and energy) fixed are shown in Fig. 5. Here, as can be seen from Table II, the $FWHM_R$ values of the four spin-flip scenarios and two transfer scenarios are 500, 500, 94, 226, 158, and 594 fs, respectively. Clearly, in each case, a deviation from $FWHM_R$ within a moderate range always causes a decrease of the fidelity. If the occupation of the final state for each scenario above 75% is considered to be acceptable, then the dynamics tolerances (i.e., the FWHM differences with respect to $FWHM_R$) of laser FWHM are about 125($l$)/–($r$), 151($l$)/–($r$), 32($l$)/29($r$), and 78($l$)/60($r$), 4($l$)/4($r$), and 6($l$)/22($r$) fs, respectively, suggesting that spin-transfer scenarios are more sensitive to FWHM than flip scenarios and thus more difficult to be realized in experiment when there is a FWHM deviation. Here the letter $l$ in the parentheses is the abbreviation for direction left, and $r$ denotes right direction.

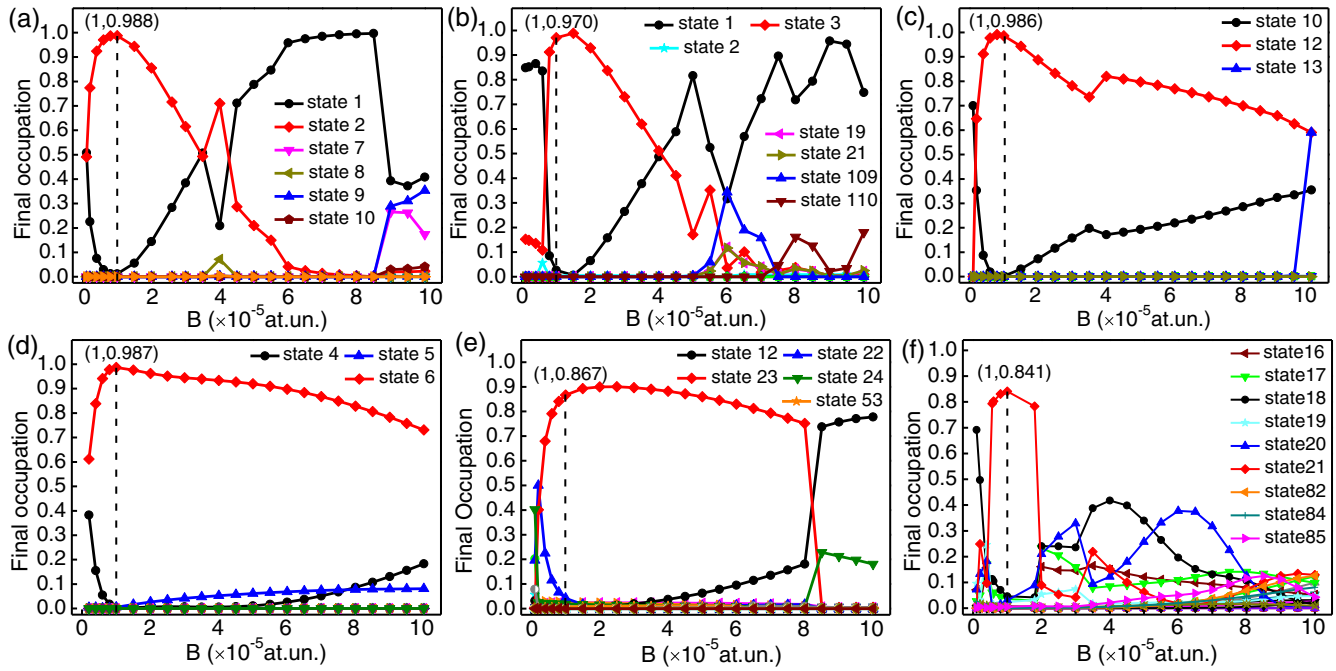


FIG. 6. The magnetic field effects on the six spin scenarios discussed in this manuscript. (a)–(d) give the magnetic-filed-dependent final occupation of the involved states of the spin-flip processes in FeBz, $FeBz_2$, $Fe_2Bz$, and $Fe_2Bz_2$, respectively, and (e) and (f) show the magnetic-filed-dependent final occupation of the involved states of the spin-transfer processes in $Fe_2Bz$ and $Fe_2Bz_2$, respectively. In each subfigure, the lines connected by solid circles and diamonds represent the change trends of the initial and final states, respectively, and others denote the FWHM-dependent final occupation of some selected intermediate states which show noticeable occupation during the spin dynamics.

One can also see that for the spin-flip scenarios in $Fe_2Bz$ and $Fe_2Bz_2$ [Figs. 5(c) and 5(d)], with the increase of FWHM, the fidelity decreases gradually first and then climbs up. Specifically, for $Fe_2Bz$, after the decrease of the fidelity from 0.986 to zero when FWHM is 188 fs, an even higher value of 0.988 is achieved when FWHM is 282 fs. For $Fe_2Bz_2$, its fidelity decays gradually from the highest value 0.987 at 226 fs to zero at 452 fs, and then has a tendency of going up. To understand this phenomenon, we first consider an ideal two-level quantum system ($|i\rangle$: initial state, $|e\rangle$: final state) driven by an oscillatory field (i.e., laser pulses in our paper). As is known, with the initial condition being set as $c_i^2|_{t=0} = 1$, the system will end entirely at the excited state at one half of the Rabi cycle at the resonant Rabi frequency (i.e., zero detuning). The target state in our spin-flip scenarios is just obtained in such a way, i.e., when the final state occupation reaches up to the greatest possible value after one-half Rabi cycle the laser pulses were turned off to leave the system in this state. If the FWHM equals an even multiple of the $FWHM_R$ value (e.g., 188 fs, which is twice the $FWHM_R$ value of 94 fs and equivalent to one Rabi cycle, as shown in Fig. 5(c)], it always gives zero fidelity (which means the system stays in its original initial state instead of the final state). If an odd multiple of the $FWHM_R$ value applies (e.g., 282 fs, which is three times of the $FWHM_R$ value of 94 fs and equivalent to one and a half Rabi cycles), it always gives an equivalent high final-state occupation as the case of $FWHM_R$. Thus, the oscillation features of the FWHM effect on the spin-flip scenario in $Fe_2Bz$ and $Fe_2Bz_2$ is quite understandable. A similar behavior can be also observed in Ref. [57], where the magnetization reversal can be induced by several combinations of pulse duration and intensity strength. Here, due to the individual encoding method for the laser in our genetic program, the values of parameters represented by the bit series are limited by the parameter range, which induces the one-way derivation of FWHM in Figs. 5(a) and 5(b).

Strikingly contrary to Figs. 5(a)–5(d), the initial and final states of the two transfer scenarios oscillate severely in a period of about 60 and 100 fs, respectively. In addition, no equivalent fidelity appears at the positions of $(2n+1) \times$ FWHM ($n = 1, 2, 3, \cdots$). Both of these features indicate the existence of the detuning from the resonant Rabi frequency in spin transfer, resulting from the large number of intermediate states involved and complicated transitions brought about.

### C. Effect of external magnetic field on ultrafast spin dynamics

Keeping the direction of the magnetic field (as well as laser parameters) to be fixed, we vary its magnitude from 0 to $1.0 \times 10^{-4}$ at.un. (i.e., in the region from 0 to 23.5 T, here at.un. is the abbreviation of atomic units) and study its influence on the six spin scenarios obtained in this paper. The results are shown in Fig. 6. The highest occupation of the target states, the change trend of which is denoted with the line connected by solid diamond symbols, mostly occur at $B = 1.0\times10^{-5}$ at.un. It can be seen that for smaller B (e.g., below $2.0\times10^{-6}$ at.un.), the desired states cannot be well populated, especially for the flip scenario where the number of the involved intermediate states is the largest [see Fig. 6(b)]

and the two transfer scenarios [see Figs. 6(e) and 6(f)]. This is due to the fact that the Zeeman splitting, required by our $\Lambda$ process, is insufficient to distinguish the states stemming from the same triplet terms. For example, for the transfer scenario of $Fe_2Bz$ at $B = 1.0\times10^{-6}$ at.un., the system mainly goes to a linear combination of states 22 and 24, which stem from the same triplet term with the originally targeted state 23. For $Fe_2Bz_2$, the system mainly goes to a linear combination of states 18 (initial state), 19 and 20, the latter two of which stem from the same triplet term with the originally targeted state 21.

On the other hand, for larger magnetic field (e.g., above $8.0 \times 10^{-5}$ at.un.), the intermediate states in each subfigure start to take noticeable occupation, causing a decrease of final occupation of the target state. This can be attributed to the Paschen-Back effect: (i) With larger magnetic field applied, the SOC of the system will become relatively weaker and the previously spin-mixed intermediate states tend to be spin pure, thus it suppresses the efficiency of the spin scenarios since a $\Lambda$ process is necessitated and facilitated by SOC. (ii) Larger magnetic field brings about stronger level crossing that may change the phase factors of the excited intermediate states and even their state ordering. The former change has a strong effect on the interference of the intermediate states during the propagation, and the latter one induces some states with the same numbering to be actually different from the initial resonant situation, both of them limit the achievement of the desired population of the target state. In fact, the magnetic strength is extended up to $4.0 \times 10^{-4}$ at.un. in our calculation. It turns out that, due to the involvement of more (mainly high-lying) intermediate states in each case, the target state is hardly populated when B is higher than $1.0 \times 10^{-4}$ at.un. Even for the cases of spin-flip scenarios in $Fe_2Bz$ and $Fe_2Bz_2$, as shown in Figs. 6(c) and 6(d) which are relatively insensitive to B, the final-state occupation both decay (from 0.6 and 0.7 at $B = 1.0 \times 10^{-4}$ at.un., respectively) rapidly to zero at $B = 2.0 \times 10^{-4}$ at.un.

One can clearly see that, from Fig. 6, the flip scenario in $Fe_2Bz_2$ is the most stable one with respect to the change of magnetic field since its final-state occupation keeps at a flat plateau with high values within a large region of the increasing magnetic field strength. This stability favors the experimental realization of the corresponding spin dynamics, while the spin-transfer scenario in the same structure turns to be the most sensitive one because the final-state occupation decreases rapidly when there is a small deviation in the field magnitude. This sensitivity can be converted to lateral resolution of a nanodevice made of such identical clusters through the introduction of an inhomogeneous magnetic field (e.g., a linear-gradient B field), and thus is beneficial to their future memory application, as mentioned in the introduction section. To illustrate this in great detail, in the following we reexamine the B-field effect of the transfer scenario in $Fe_2Bz_2$ in the one-dimensional case, and expand the dependence of fidelity on magnetic field to that on magnetic field and spatial location.

The results are shown in Fig. 7, in which the linear-gradient magnetic field is denoted by the line $B = kx$, with the ranges of the spatial length and magnetic-field strength chosen from 0 to 2350 nm and from 0 to 23.5 T, respectively. The values denoted along the line are the field-dependent fidelity.

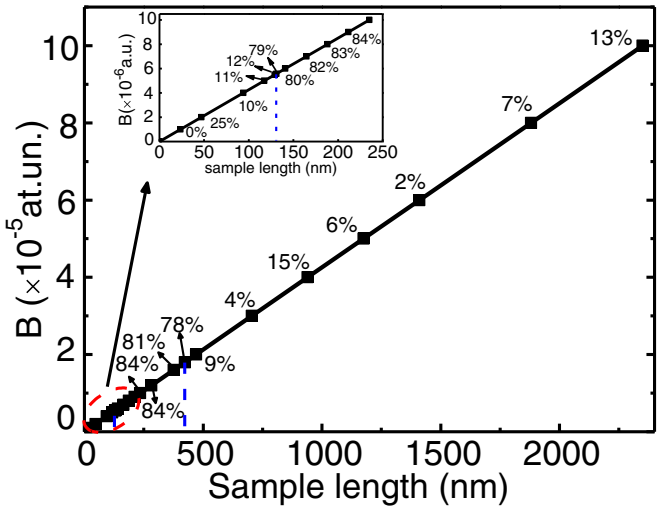


FIG. 7. Determination of the lateral resolution of a device sample made of homogeneous $Fe_2Bz_2$ clusters by introducing a linear-gradient magnetic field (with a gradient value of 10 T/$\mu$m) on the predicted ultrafast spin-transfer scenarios. The field-fidelity correspondence is taken from Fig. 6(f). When varying the field strength from 0 to $1.0 \times 10^{-4}$ at.un. (23.5 T), the corresponding sample length the magnetic field acts on is 2350 nm. The intensive field-dependent fidelity values below $1.0 \times 10^{-5}$ at.un. (i.e., 2.35 T) is shown in the inset.

Compared to Fig. 6(f), several fidelity values below $2 \times 10^{-5}$ are added for the purpose of obtaining a more precise level of sensitivity, and the values for the higher field region are selectively shown. Here it should be noted that, when we apply a magnetic field with strength varying from 0 to $1 \times 10^{-4}$ at.un. (23.5 T) on a nanoscale sample, a large gradient is needed. Nowadays, the maximal reachable B-field gradient values of the order of $1 - 10$ T/$\mu$m have been obtained on various materials (such as nanoscale Dy stripes, mircopatterned permalloy-Co films, and Nd-Fe-B films) with the aid of modern micro- and nanotechnologies [61–66], and have been used to investigate the coherent manipulation of individual electron spin, the hyperfine-induced spin dephasing, and the effects on biological elements (cells and molecules) [67–69]. Thus, a typical gradient value of 10 T/$\mu$m is chosen here, and the corresponding spatial expansion is around 2350 nm for the B-field range from 0 to 23.5 T. Obviously, from Fig. 7 one can see that the fidelity of the spin-transfer scenario is always above 78% when the field strength lies in the range from $5.58 \times 10^{-6}$ to $1.8 \times 10^{-5}$ at.un. (i.e., from 1.31 to 4.23 T), as confined by the two blue dashed lines. Correspondingly, the active spatial region is from 131 to 423 nm, indicating a spatially resolved length of around 300 nm. For our results, if we take advantage of the abrupt deterioration of the spin scenario of Fig. 6(f), for which a decrease of the magnetic field by 0.47 T (i.e., from $6 \times 10^{-6}$ to $4 \times 10^{-6}$ at.un.) or an increase of the magnetic field by 0.94 T (i.e., from $1.6 \times 10^{-5}$ to $2 \times 10^{-5}$ at.un.) leads to a fidelity from more than 80% to less than 10%, and combining with a 10 T/$\mu$m gradient, we arrive at a spatial resolution of the order of 47 or 94 nm. These numbers are at least a factor of two smaller than the one of a standard optical microscope (200–600 nm [70]). In the case of

a higher-gradient magnetic field or a molecule which is much more sensitive to the magnetic-field strength, this resolution can be expected to be highly improved for the high-density recording capability of B-field assisted magnetic recording.

## V. SUMMARY

To summarize, we present a first-principles study on the laser-induced ultrafast spin dynamics in clusters $Fe_mBz_n$ $(m, n = 1, 2)$. Their structural and energetic properties are compared, and the possible influence on the spin-flip scenarios are addressed. A CT state involving spin-transfer scenario completed within 500 fs is found in $Fe_2Bz$. As expected, its time duration is much faster than the ordinary transfer dynamics achieved in $Fe_2Bz_2$. The reversibility of the scenarios are found to be mainly determined by the (a)symmetric feature of the dynamics behavior, the number of the involved intermediate states, and the (un)balanced properties of the two subbranches of the $\Lambda$ process. In a large part of our paper, we investigate the effects of laser FWHM and the magnitude of the external magnetic field on the proposed spin scenarios, and analyze the stability and sensitivity of each scenario. We find that, due to the large detuning from the resonant Rabi frequencies, spin-transfer scenarios have smaller tolerance values than spin-flip scenarios with respect to the laser FWHM, indicating their sensitivity to this parameter. For the effects of magnetic field strength, the fidelity of each scenario is always suppressed when B is smaller than $1.0 \times 10^{-6}$ at.un. (due to the indistinguishability of the states) and larger than $8.0 \times 10^{-5}$ at.un. (due to the Paschen-Back effect). Based on this effect, the idea of magnetic field stressing for the possible memory application is proposed. All these theoretical predictions are expected to provide valuable information for the experimental probe of ultrafast laser control magnetism on the organic-TM clusters and their future precise information storage and molecular spintronics device applications.

## ACKNOWLEDGMENTS

We acknowledge financial support from the National Natural Science Foundation of China (No. 11504223, No. 11572251, and No. 11872309), Natural Science Basic Research Plan in Shaanxi Province (No. 2017JM1033), the Fundamental Research Funds for the Central Universities (No. GK201903015 and No. 3102017JC01003), and the German Research Foundation (Deutsche Forschungsgemeinschaft, DFG) through the Transregional Collaborative Research Center SFB/TRR 173 "Spin+X".

## APPENDIX

Compared to other work, the ground-state spin multiplicities of the structures calculated in this paper agree with Refs. [26,28–30,32–34,71]. However, their symmetries may differ due to the different isomers and computational methods used. For example, for FeBz, $C_{6v}$ and $C_{2v}$ configurations are respectively suggested in Refs. [26,28–30,32,34]. Our calculation gives a $C_1$ configuration, which is lower than the $C_{6v}$ (with two large imaginary modes) and $C_{2v}$ configurations by 0.995 eV and 0.001 eV, respectively. For $FeBz_2$, a symmetry of $D_{6h}$ is proposed in Refs. [26,29,30,32,71], while our HF calculations, without any symmetry constraint of either the Bz ring or the whole structure, favor the $C_{2v}$ configuration, which is 4.095 eV lower than the $D_{6h}$ one.

TABLE III. The Fe-Fe and Fe-C bond lengths of the four optimized structures.

| Cluster | Bond length (in Å) | |
|---|---|---|
| FeBz | Fe1-C1 = 2.4215 | Fe1-C2 = 2.4227 |
| | Fe1-C3 = 2.4000 | Fe1-C4 = 2.4004 |
| | Fe1-C5 = 2.4225 | Fe1-C6 = 2.4217 |
| $FeBz_2$ | Fe1-C1/C6 = 2.3623 | |
| | Fe1-C2/C3/C4/C5 = 2.3904 | |
| | Fe1-C7/C12 = 2.3628 | |
| | Fe1-C8/C9/C10/C11 = 2.3910 | |
| $Fe_2Bz$ | Fe1-Fe2 = 2.7135 | Fe1-C1/C6 = 2.3775 |
| | Fe1-C2/C3/C4/C5 = 2.3576 | |
| | Fe1-Fe2 = 2.3842 | Fe1-C1/C6 = 2.4218 |
| | Fe1-C2/C4 = 2.4222 | Fe1-C3/C5 = 2.4171 |
| $Fe_2Bz_2$ | Fe2-C7/C12 = 2.5766 | Fe2-C8/C10 = 2.5631 |
| | Fe2-C9/C11 = 2.6282 | |

Different from the tilted upright (i.e., Fe-Fe bond deviates by some angle from a perpendicular direction to the Bz plane) geometry proposed in Refs. [32,33], the most stable conformation of $Fe_2Bz$ in our calculation is a triplet upright one, which is lower than the stable triplet parallel configuration (i.e., Fe-Fe bond is parallel to the Bz plane) by 1.763 eV, in line with Refs. [28,31]. A stable titled upright configuration deviated by 34.4° is also obtained, but only under a loose convergence criteria of $10^{-7}$ at.un. The most stable geometry of $Fe_2Bz_2$ (which was suggested by Ref. [26] that both the perpendicular and coaxial geometries are possible) we obtain is a coaxial (i.e., Fe-Fe bond is almost parallel to the line connecting to the centers of the two Bzs) structure with multiplicity 3, which is lower than the stable quintet perpendicular (i.e., Fe-Fe bond is nearly perpendicular to the line connecting to the centers of the two Bzs) configuration [32] by 0.914 eV. An even lower-energy structure for a quintet coaxial configuration under lower convergence criterion is also found, but there is one inevitable imaginary mode with a value of $-8.9$ $cm^{-1}$, indicating its instability. The converged triplet perpendicular one cannot be achieved.

Table III lists the Fe-Fe and Fe-C bond lengths of the four optimized structures. It can be seen that, with an additional Bz molecule, the Fe-Fe bond length of $Fe_2Bz_2$ (2.3842 Å) turns to be shorter than that of $Fe_2Bz$ (2.7135 Å). This results from the fact that the attachment of a Bz ring leads to a loss of $3d$ electrons per Bz attached [72] and thus reduces the repulsion of the Fe dimer. On the other hand, due to the addition of an iron atom that brings about strong repulsion of the Fe dimer, the distance between Fe1 and the center of the Bz ring of $Fe_2Bz$ (1.8837 Å) becomes shorter than that of FeBz (2.0084 Å). For the bonding parameters related to the Bz rings, the C–C bond lengths range from 1.4014 Å to 1.4144 Å, and the C–H bond lengths range from 1.0822 Å to 1.0851 Å. Compared to the

TABLE IV. The main vibrational modes of the four clusters together with their infrared intensities. Here two degenerate modes exist for the carbon ring distortion.

| | Clusters | | | |
|---|---|---|---|---|
| Vibrational mode | FeBz | $FeBz_2$ | $Fe_2Bz$ | $Fe_2Bz_2$ |
| Out-of-plane C–H bend | 698(82.2) | 706 (154.8) | 697(122.1) | 673 (153.2) |
| Benzene ring breathing | 922(22.3) | 920 (71.0) | 913(37.6) | 918(53.6) |
| Carbon ring distortion | 1395(40.5), 1399(44.5) | 1390 (90.1), 1396 (58.9) | 1383(29.7), 1386(24.5) | 1389(28.3), 1395(38.2) |
| C–H stretching | 3063 (73.0) | 3078 (422.1) | 3055(65.8) | 3066(77.7) |

experimental values of 673, 1038, 1486, 3047.3 $cm^{-1}$ for the modes of out-of-plane C–H bend, carbon-ring distortion, Bz ring breathing, and C–H stretching of the gas-phase Bz ring [73], our calculations show decent agreements, as can be seen in Table IV. In addition, the values of Bz ring breathing ($913 - 922$ $cm^{-1}$) and carbon-ring distortion ($1383 - 1399$ $cm^{-1}$) in our paper are all redshifted, and the values of out-of-plane C–H bend ($673 - 706$ $cm^{-1}$) and C–H stretching modes ($3055 - 3078$ $cm^{-1}$) are all blueshifted. These are consistent with the tendency of Refs. [25,33,41]. Since Fe is much heavier than C and H, its related Fe-Bz vibrational frequencies with noticeable intensities lie within the region of $27.8 \sim 280.2$ $cm^{-1}$, which are much smaller than the related Bz ring modes.


[1] L. Bogani and W. Wernsdorfer, Nat. Mater. **7**, 179 (2008).
[2] A. R. Rocha, V. M. García-Suárez, S. W. Bailey, C. J. Lambert, J. Ferrer, and S. Sanvito, Nat. Mater. **4**, 335 (2005).
[3] A. Ardavan, O. Rival, J. J. L. Morton, S. J. Blundell, A. M. Tyryshkin, G. A. Timco, and R. E. P. Winpenny, Phys. Rev. Lett. **98**, 057201 (2007).
[4] G. D. Mahan, Phys. Rev. Lett. **102**, 016801 (2009).
[5] F. Luis, A. Repollés, M. J. Martínez-Pérez, D. Aguilà, O. Roubeau, D. Zueco, P. J. Alonso, M. Evangelisti, A. Camón, J. Sesé, L. A. Barrios, and G. Aromí, Phys. Rev. Lett. **107**, 117203 (2011).
[6] A. A. Khajetoorians and A. J. Heinrich, Science **352**, 296 (2016).
[7] F. D. Natterer, K. Yang, W. Paul, P. Willke, T. Choi, T. Greber, A. J. Heinrich, and C. P. Lutz, Nature **543**, 226 (2017).
[8] E. Beaurepaire, J.-C. Merle, A. Daunois, and J.-Y. Bigot, Phys. Rev. Lett. **76**, 4250 (1996).
[9] G. P. Zhang and W. Hübner, Phys. Rev. Lett. **85**, 3025 (2000).
[10] B. Koopmans, J. J. M. Ruigrok, F. Dalla Longa, and W. J. M. de Jonge, Phys. Rev. Lett. **95**, 267207 (2005).
[11] C. D. Stanciu, A. Tsukamoto, A. V. Kimel, F. Hansteen, A. Kirilyuk, A. Itoh, and T. Rasing, Phys. Rev. Lett. **99**, 217204 (2007).
[12] J.-Y. Bigot, M. Vomir, and E. Beaurepaire, Nat. Phys. **5**, 515 (2009).
[13] G. Lefkidis, G. P. Zhang, and W. Hübner, Phys. Rev. Lett. **103**, 217401 (2009).
[14] A. Kirilyuk, A. V. Kimel, and T. Rasing, Rev. Mod. Phys. **82**, 2731 (2010).
[15] U. Atxitia and O. Chubykalo-Fesenko, Phys. Rev. B **84**, 144414 (2011).
[16] T. Roth, A. J. Schellekens, S. Alebrand, O. Schmitt, D. Steil, B. Koopmans, M. Cinchetti, and M. Aeschlimann, Phys. Rev. X **2**, 021006 (2012).
[17] B. Pfau, S. Schaffert, L. Müller, C. Gutt, A. Al-Shemmary, F. Büttner, R. Delaunay, S. Düsterer, S. Flewett, R. Frömter *et al.*, Nat. Commun. **3**, 1100 (2012).
[18] A. Eschenlohr, M. Battiato, P. Maldonado, N. Pontius, T. Kachel, K. Holldack, R. Mitzner, A. Föhlisch, P. M. Oppeneer, and C. Stamm, Nat. Mater. **12**, 332 (2013).
[19] C.-H. Lambert, S. Mangin, B. S. D. C. S. Varaprasad, Y. K. Takahashi, M. Hehn, M. Cinchetti, G. Malinowski, K. Hono, Y. Fainman, M. Aeschlimann, and E. E. Fullerton, Science **345**, 1337 (2014).
[20] O. Morandi and P.-A. Hervieux, Phys. Rev. B **96**, 024441 (2017).
[21] T. J. Kealy and P. L. Pauson, Nature **168**, 1039 (1951).
[22] T. Kurikawa, H. Takeda, M. Hirano, K. Judai, T. Arita, S. Nagao, A. Nakajima, and K. Kaya, Organometallics **18**, 1430 (1999).
[23] C. S. Feigerle, S. Bililign, and J. C. Miller, J. Nanopart. Res. **2**, 147 (2000).
[24] A. Nakajima and K. Kaya, J. Phys. Chem. A **104**, 176 (2000).
[25] T. D. Jaeger, D. van Heijnsbergen, S. J. Klippenstein, G. von Helden, G. Meijer, and M. A. Duncan, J. Am. Chem. Soc. **126**, 10981 (2004).
[26] W. J. Zheng, S. N. Eustis, X. Li, J. M. Nilles, O. C. Thomas, K. H. Bowen, and A. K. Kandalam, Chem. Phys. Lett. **462**, 35 (2008).
[27] M. A. Duncan, Int. J. Mass. Spectrom. **272**, 99 (2008).
[28] S. F. Parker, J. Phys. Chem. A **114**, 1657 (2010).
[29] Y. Wang, J. Szczepanski, and M. Vala, Chem. Phys. **342**, 107 (2007).
[30] R. Pandey, B. K. Rao, P. Jena, and M. A. Blanco, J. Am. Chem. Soc. **123**, 3799 (2001).
[31] R. J. Xiao, D. Fritsch, M. D. Kuz'min, K. Koepernik, M. Richter, K. Vietze, and G. Seifert, Phys. Rev. B **82**, 205125 (2010).
[32] I. Valencia and M. Castro, Phys. Chem. Chem. Phys. **12**, 7545 (2010).
[33] I. Valencia, Chem. Phys. **476**, 46 (2016).
[34] R. Pandey, B. K. Rao, P. Jena, and J. M. Newsam, Chem. Phys. Lett. **321**, 142 (2000).
[35] R. Flores, H. F. Cortes, and M. Castro, J. Mol. Struct. **1103**, 295 (2016).

[36] J. W. Buchanan, G. A. Grieves, J. E. Reddic, and M. A. Duncan, Int. J. Mass. Spectrom. **182**, 323 (1999).

[37] X. Li, S. Eustis, K. H. Bowen, A. K. Kandalam, and P. Jena, J. Chem. Phys. **129**, 074313 (2008).

[38] X. Li, K. H. Bowen, P. Jena, and A. K. Kandalam, J. Chem. Phys. **135**, 204301 (2011).

[39] H. Johll, H. C. Kang, and E. S. Tok, Phys. Rev. B **79**, 245416 (2009).

[40] H. Johll, J. Wu, S. W. Ong, H. C. Kang, and E. S. Tok, Phys. Rev. B **83**, 205408 (2011).

[41] L. Y. Zhu, T. T. Zhang, M. X. Yi, and J. L. Wang, J. Phys. Chem. A **114**, 9398 (2010).

[42] R. Masrour, A. Jabar, M. Hamedoun, A. Benyoussef, and E. K. Hlil, J. Magn. Magn. Mater. **432**, 318 (2017).

[43] V. V. Maslyuk, A. Bagrets, V. Meded, A. Arnold, F. Evers, M. Brandbyge, T. Bredow, and I. Mertig, Phys. Rev. Lett. **97**, 097201 (2006).

[44] H. J. Xiang, J. L. Yang, J. G. Hou, and Q. S. Zhu, J. Am. Chem. Soc. **128**, 2310 (2006).

[45] L. Horváthová, R. Derian, L. Mitas, and I. Štich, Phys. Rev. B **90**, 115414 (2014).

[46] R. Gómez-Abal and W. Hübner, Phys. Rev. B **65**, 195114 (2002).

[47] N. Zhang, H. Du, J. Chang, W. Jin, C. Li, G. Lefkidis, and W. Hübner, Phys. Rev. B **98**, 104431 (2018).

[48] C. Li, W. Jin, H. P. Xiang, G. Lefkidis, and W. Hübner, Phys. Rev. B **84**, 054415 (2011).

[49] W. Jin, C. Li, G. Lefkidis, and W. Hübner, Phys. Rev. B **89**, 024419 (2014).

[50] M. J. Frisch, G. W. Trucks, H. B. Schlegel, G. E. Scuseria, M. A. Robb, J. R. Cheeseman, G. Scalmani, V. Barone, G. A. Petersson, H. Nakatsuji, X. Li, M. Caricato, A. V. Marenich, J. Bloino, B. G. Janesko, R. Gomperts, B. Mennucci, H. P. Hratchian, J. V. Ortiz, A. F. Izmaylov, J. L. Sonnenberg, D. Williams-Young, F. Ding, F. Lipparini, F. Egidi, J. Goings, B. Peng, A. Petrone, T. Henderson, D. Ranasinghe, V. G. Zakrzewski, J. Gao, N. Rega, G. Zheng, W. Liang, M. Hada, M. Ehara, K. Toyota, R. Fukuda, J. Hasegawa, M. Ishida, T. Nakajima, Y. Honda, O. Kitao, H. Nakai, T. Vreven, K. Throssell, J. A. Montgomery, Jr., J. E. Peralta, F. Ogliaro, M. J. Bearpark, J. J. Heyd, E. N. Brothers, K. N. Kudin, V. N. Staroverov, T. A. Keith, R. Kobayashi, J. Normand, K. Raghavachari, A. P. Rendell, J. C. Burant, S. S. Iyengar, J. Tomasi, M. Cossi, J. M. Millam, M. Klene, C. Adamo, R. Cammi, J. W. Ochterski, R. L. Martin, K. Morokuma, O. Farkas, J. B. Foresman, and D. J. Fox, Gaussian16 Revision B.01 (Gaussian Inc., Wallingford, CT, 2016).

[51] H. Nakatsuji, Chem. Phys. Lett. **67**, 329 (1979).

[52] D. Chaudhuri, H. P. Xiang, G. Lefkidis, and W. Hübner, Phys. Rev. B **90**, 245113 (2014).

[53] D. Dutta, M. Becherer, D. Bellaire, F. Dietrich, M. Gerhards, G. Lefkidis, and W. Hübner, Phys. Rev. B **97**, 224404 (2018).

[54] Y. Pavlyukh, E. Rentschler, H. J. Elmers, W. Hübner, and G. Lefkidis, Phys. Rev. B **97**, 214408 (2018).

[55] J. R. Cash and A. H. Karp, ACM Trans. Math. Softw. **16**, 201 (1990).

[56] T. Hartenstein, C. Li, G. Lefkidis, and W. Hübner, J. Phys. D: Appl. Phys. **41**, 164006 (2008).

[57] G. Lefkidis and W. Hübner, Phys. Rev. B **76**, 014418 (2007).

[58] W. Jin, M. Becherer, D. Bellaire, G. Lefkidis, M. Gerhards, and W. Hübner, Phys. Rev. B **89**, 144409 (2014).

[59] D. Chaudhuri, W. Jin, G. Lefkidis, and Hübner, J. Chem. Phys. **143**, 174303 (2015).

[60] G. P. Zhang, W. Hübner, G. Lefkidis, Y. H. Bai, and T. F. George, Nat. Phys. **5**, 499 (2009).

[61] J. Wróbel, T. Dietl, A. Łusakowski, G. Grabecki, K. Fronc, R. Hey, K. H. Ploog, and H. Shtrikman, Phys. Rev. Lett. **93**, 246601 (2004).

[62] M. Pioro-Ladrière, T. Obata, Y. Tokura, Y.-S. Shin, T. Kubo, K. Yoshida, T. Taniyama, and S. Tarucha, Nat. Phys. **4**, 776 (2008).

[63] M. Kustov, P. Laczkowski, D. Hykel, K. Hasselbach, F. Dumas-Bouchiat, D. O'Brien, P. Kauffmann, R. Grechishkin, D. Givord, G. Reyne, O. Cugat, and N. M. Dempsey, J. Appl. Phys. **108**, 063914 (2010).

[64] H. J. Mamin, C. T. Rettner, M. H. Sherwood, L. Gao, and D. Rugar, Appl. Phys. Lett. **100**, 013102 (2012).

[65] B. Schüler, M. Cerchez, H. Xu, J. Schluck, T. Heinzel, D. Reuter, and A. D. Wieck, Phys. Rev. B **90**, 201111(R) (2014).

[66] N. M. Dempsey, D. L. Roy, H. Marelli-Mathevon, G. Shaw, A. Dias, R. B. G. Kramer, L. V. Cuong, M. Kustov, L. F. Zanini, C. Villard, K. Hasselbach, C. Tomba, and F. Dumas-Bouchiat, Appl. Phys. Lett. **104**, 262401 (2014).

[67] T. Obata, M. Pioro-Ladrière, Y. Tokura, Y.-S. Shin, T. Kubo, K. Yoshida, T. Taniyama, and S. Tarucha, Phys. Rev. B **81**, 085317 (2010).

[68] F. Beaudoin and W. A. Coish, Phys. Rev. B **88**, 085320 (2013).

[69] V. Zablotskii, O. Lunov, S. Kubinova, T. Polyakova, E. Sykova, and A. Dejneka, J. Phys. D: Appl. Phys. **49**, 493003 (2016).

[70] C. Cremer and B. R. Masters, Eur. Phys. J. H **38**, 281 (2013).

[71] D. Ghosh, P. Parida, and S. K. Pati, J. Phys. Chem. C **116**, 18487 (2012).

[72] M. Karolak and D. Jacob, J. Phys: Condens. Matter **28**, 445301 (2016).

[73] T. Shimanouchi, Molecular vibrational frequencies, in *NIST Chemistry WebBook, NIST Standard Reference Database Number 69*, edited by P. J. Lingstrom and W. G. Mallard (National Institute of Standards and Technology, Gaithersburg MD, retrieved April 16, 2019), https://doi.org/10.18434/T4D303.